Magnetic vortex-antivortex crystals generated by spin-polarized current

Yuri Gaididei,[1] Oleksii M. Volkov,[2] Volodymyr P. Kravchuk,[1] and Denis D. Sheka[2,*]
[1]*Bogolyubov Institute for Theoretical Physics, 03143 Kiev, Ukraine*
[2]*Taras Shevchenko National University of Kiev, 01601 Kiev, Ukraine*
(Received 27 July 2012; published 3 October 2012)

We study vortex pattern formation in thin ferromagnetic films under the action of strong spin-polarized currents. Considering the currents which are polarized along the normal of the film plane, we determine the critical current above which the film goes to a saturated state with all magnetic moments being perpendicular to the film plane. We show that stable square vortex-antivortex superlattices (*vortex crystals*) appear slightly below the critical current. The melting of the vortex crystal occurs with further decrease of current. A mechanism of current-induced periodic vortex-antivortex lattice formation is proposed. Micromagnetic simulations confirm our analytical results with a high accuracy.

DOI: 10.1103/PhysRevB.86.144401 PACS number(s): 75.10.Hk, 75.40.Mg, 05.45.−a, 72.25.Ba

I. INTRODUCTION

Use of the spin-polarized current is a convenient means to handle magnetization states of nanomagnets without application of an external magnetic field.[1] This is of high importance for constructing purely current controlled devices.[2,3] One effective way to influence film magnetization by the spin-polarized current is to use the pillar structure, where the current flows perpendicularly to the magnetic film.[4–9] Special efforts have been made to explore the possibility to control the properties of a magnetic vortex[10–20] because the latter is a convenient carrier of bits of information. The theoretical study of this is based on the Slonczewski-Berger model.[21–23]

In this paper we focus on the problem of regular pattern formation (vortex-antivortex superlattice) under the action of strong spin-polarized currents, which precedes saturation. Superstructures of vortices are known from Kelvin's fluid vortices.[24] Nowadays, superlattices of vortices are known in superconductivity,[25] superfluidity,[26] Bose-Einstein condensates (rotating,[27] nonrotating,[28] optically dressing condensate[29]), and optics.[30–32] Vortexlike superstructures appear also in magnetism: Skyrmion crystals were predicted in chiral magnets,[33] which is now well-confirmed experimentally,[34–36] and a vortex-antivortex lattice (chirality waves) appears in the Kondo lattice model.[37] Recently, we found vortex-antivortex superlattices (*vortex crystals*) in nanomagnets under the action of strong spin-polarized currents.[38] Using micromagnetic simulations, we found that crystallization precedes saturation: Square superlattices were observed for a range of current densities in the immediate vicinity of J_c, which is the critical current which saturates the magnetization along its direction.[38] Here we prove theoretically the possibility of vortex-antivortex superlattices in ordinary isotropic magnetic film. To this end, we build the full theory of saturation of a thin ferromagnetic film by use of a transverse spin-polarized current. In particular, we show that loss of stability of the saturated state leads to the appearance of stable square vortex crystals.

The paper is organized as follows: In Sec. II we describe the model and our approach. The linear analysis (Sec. III) enables us to obtain the value of the saturation current J_c as a function of the material parameters and film thickness. The nonlinear analysis (Sec. IV) proves the possibility of stable square vortex-antivortex superlattices in a presaturated regime. We verify the obtained analytical results with micromagnetic simulations (Sec. V). In addition, using the simulations, we describe the transition from crystal phase into fluid phase which appears with a decrease of current density.

II. MODEL AND DISCRETE DESCRIPTION

We consider here a soft magnetic film with thickness h and lateral size $L \gg h$. We model magnetization of the film as a three-dimensional cubic lattice of magnetic moments $\boldsymbol{M}_{\boldsymbol{\nu}}$ with lattice spacing $a \ll h$, where $\boldsymbol{\nu} = a(\nu_x, \nu_y, \nu_z)$ with $\nu_x, \nu_y, \nu_z \in \mathbb{Z}$ is a three-dimensional index.[39] In the following, we use the notations $\mathcal{N}_z = h/a$ and $\mathcal{N}_{xy} = L^2/a^2$ for the number of magnetic moments along the thickness and within the film plane, respectively. We assume also that the magnetization of the film is uniform along the thickness. That enables us to base our study on the two-dimensional discrete Landau-Lifshitz-Slonczewski equation,[21–23]

$$\dot{\boldsymbol{m}}_{\boldsymbol{n}} = \boldsymbol{m}_{\boldsymbol{n}} \times \partial \mathcal{E}/\partial \boldsymbol{m}_{\boldsymbol{n}} - j\varepsilon \boldsymbol{m}_{\boldsymbol{n}} \times [\boldsymbol{m}_{\boldsymbol{n}} \times \hat{\boldsymbol{z}}], \qquad (1)$$

which describes the magnetization dynamics under influence of a spin-polarized current which flows perpendicularly to the magnet plane, along the $\hat{\boldsymbol{z}}$ axis. It is also assumed that the current flow and its spin polarization are of the same direction in (1). The two-dimensional index $\boldsymbol{n} = a(n_x, n_y)$ with $n_x, n_y \in \mathbb{Z}$ numerates the normalized magnetic moments $\boldsymbol{m}_{\boldsymbol{n}} = \boldsymbol{M}_{\boldsymbol{n}}/|\boldsymbol{M}_{\boldsymbol{n}}|$ within the film plane. The overdot indicates the derivative with respect to the rescaled time in units of $(4\pi\gamma M_s)^{-1}$, γ is the gyromagnetic ratio, M_s is the saturation magnetization, and $\mathcal{E} = E/(4\pi M_s^2 a^3 \mathcal{N}_z)$ is dimensionless magnetic energy. The normalized electrical current density $j = J/J_0$, where $J_0 = M_s^2|e|h/\hbar$, with e being the electron charge and $\hbar$ being the Planck constant. The spin-transfer torque efficiency function ε has the form $\varepsilon = \eta\Lambda^2/[(\Lambda^2+1) + (\Lambda^2-1)(\boldsymbol{m}\cdot\hat{\boldsymbol{z}})]$, where η is the degree of spin polarization and parameter $\Lambda \geqslant 1$ describes the mismatch between the spacer and the ferromagnet resistance.[23,40] To simplify representation, we omitted damping in the equation of motion (1), since the role of damping is not essential for crystallization of vortices; moreover, the saturation current does not depend on the damping constant.[38]

The total energy of the system $E = E_{\rm ex} + E_{\rm d}$ consists of two parts: exchange and dipole-dipole contributions. The exchange energy has the form

$$E_{\rm ex} = -\mathcal{S}^2 \mathcal{N}_z \sum_{\boldsymbol{n},\boldsymbol{l}\neq\boldsymbol{0}} \mathcal{J}_{\boldsymbol{l}} \boldsymbol{m}_{\boldsymbol{n}} \cdot \boldsymbol{m}_{\boldsymbol{n}+\boldsymbol{l}}, \tag{2}$$

where $\boldsymbol{n}$, $\boldsymbol{l}$ are two-dimensional indexes, $\mathcal{S}$ is value of spin of a ferromagnetic atom, and $\mathcal{J}_{\boldsymbol{l}}$ denotes the exchange integral between atoms distanced on $\boldsymbol{l}$.

The energy of dipole-dipole interaction is

$$E_{\rm d} = \frac{M_s^2 a^6}{2} \sum_{\boldsymbol{\nu}\neq\boldsymbol{\lambda}} \left[\frac{(\boldsymbol{m}_{\boldsymbol{\nu}} \cdot \boldsymbol{m}_{\boldsymbol{\lambda}})}{|\boldsymbol{\lambda}-\boldsymbol{\nu}|^3} - 3\frac{(\boldsymbol{m}_{\boldsymbol{\nu}} \cdot (\boldsymbol{\lambda}-\boldsymbol{\nu}))\,(\boldsymbol{m}_{\boldsymbol{\lambda}} \cdot (\boldsymbol{\lambda}-\boldsymbol{\nu}))}{|\boldsymbol{\lambda}-\boldsymbol{\nu}|^5} \right], \tag{3}$$

where $\boldsymbol{\lambda}$ and $\boldsymbol{\nu}$ are three-dimensional indexes.

By introducing the complex variable

$$\psi_{\boldsymbol{n}} = \frac{m_{\boldsymbol{n}}^x + i m_{\boldsymbol{n}}^y}{\sqrt{1+m_{\boldsymbol{n}}^z}}, \tag{4}$$

one can write the Eq. (1) in the form

$$i\dot{\psi}_{\boldsymbol{n}} = -\frac{\partial \mathcal{E}}{\partial \psi_{\boldsymbol{n}}^*} - i\varkappa \frac{1-\frac{1}{2}|\psi_{\boldsymbol{n}}|^2}{1-\frac{\xi}{2}|\psi_{\boldsymbol{n}}|^2}\psi_{\boldsymbol{n}}, \tag{5}$$

where $\varkappa = j\eta/2$ is the renormalized current, $\xi = 1-\Lambda^{-2}$, and ψ^* denotes the complex conjugation of ψ.

It is well known that, in the absence of driving ($\varkappa = 0$), the spatially homogeneous state with all moments lying in the xy plane (easy-plane magnetic state) is the most energetically favorable state of a thin ferromagnetic film. On the other hand, as seen from Eqs. (2), (3), and (5), for large positive $\varkappa$ the stationary state of the system corresponds to $\psi_{\boldsymbol{n}} = 0$ or, in other words, the system goes to the state when all magnetic moments are oriented along the z axis (saturated state). This means that there should exist a critical current $\varkappa_c$ below which the saturated state loses its stability. Our goal is to study the behavior of the system near the threshold of stability of the saturated state. Near the threshold $m_{\boldsymbol{n}}^z \lesssim 1$ and $|\psi_{\boldsymbol{n}}| \ll 1$, hence, one can expand components of the magnetization vector into a series in a way similar to the representation in terms of the Bose operators,[41]

$$\begin{aligned} m_{\boldsymbol{n}}^x &= \frac{\psi_{\boldsymbol{n}} + \psi_{\boldsymbol{n}}^*}{\sqrt{2}}\left(1 - \frac{|\psi_{\boldsymbol{n}}|^2}{4}\right) + \mathcal{O}(|\psi_{\boldsymbol{n}}|^5), \\ m_{\boldsymbol{n}}^y &= \frac{\psi_{\boldsymbol{n}} - \psi_{\boldsymbol{n}}^*}{i\sqrt{2}}\left(1 - \frac{|\psi_{\boldsymbol{n}}|^2}{4}\right) + \mathcal{O}(|\psi_{\boldsymbol{n}}|^5), \\ m_{\boldsymbol{n}}^z &= 1 - |\psi_{\boldsymbol{n}}|^2. \end{aligned} \tag{6}$$

Substituting (6) into (5), one obtains the equation of motion accurate to terms of the third order,

$$i\dot{\psi}_{\boldsymbol{n}} = -\frac{\partial \mathcal{E}}{\delta \psi_{\boldsymbol{n}}^*} - i\varkappa\psi_{\boldsymbol{n}}\left(1 - \frac{1}{2\Lambda^2}|\psi_{\boldsymbol{n}}|^2\right). \tag{7}$$

For future analysis, it is convenient to proceed to the wave-vector representation using the two-dimensional discrete Fourier transform

$$\psi_{\boldsymbol{n}} = \frac{1}{\sqrt{\mathcal{N}_{xy}}} \sum_{\boldsymbol{k}} \hat{\psi}_{\boldsymbol{k}} e^{i\boldsymbol{k}\cdot\boldsymbol{n}}, \tag{8a}$$

$$\hat{\psi}_{\boldsymbol{k}} = \frac{1}{\sqrt{\mathcal{N}_{xy}}} \sum_{\boldsymbol{n}} \psi_{\boldsymbol{n}} e^{-i\boldsymbol{k}\cdot\boldsymbol{n}}, \tag{8b}$$

with the orthogonality condition

$$\sum_{\boldsymbol{n}} e^{i(\boldsymbol{k}-\boldsymbol{k}')\cdot\boldsymbol{n}} = \mathcal{N}_{xy}\Delta(\boldsymbol{k}-\boldsymbol{k}'), \tag{9}$$

where $\boldsymbol{k} = (k_x, k_y) \equiv \frac{2\pi}{L}(l_x, l_y)$ is a two-dimensional discrete wave vector, $l_x, l_y \in \mathbb{Z}$, and $\Delta(\boldsymbol{k})$ is the Kronecker delta. Applying (8) to Eq. (7) one obtains the equation of motion in reciprocal space,

$$-i\dot{\hat{\psi}}_{\boldsymbol{k}} = \frac{\partial \mathcal{E}}{\partial \hat{\psi}_{\boldsymbol{k}}^*} + i\frac{\partial \mathcal{F}}{\partial \hat{\psi}_{\boldsymbol{k}}^*}, \tag{10}$$

where the dimensionless energy of the system can be represented as a sum,

$$\mathcal{E} = \underbrace{\mathcal{E}_{\rm ex}^0 + \mathcal{E}_{\rm d}^0}_{\mathcal{E}^0} + \underbrace{\mathcal{E}_{\rm ex}^{\rm nl} + \mathcal{E}_{\rm d}^{\rm nl}}_{\mathcal{E}^{\rm nl}}. \tag{11}$$

Here the term $\mathcal{E}^0 = \mathcal{E}_{\rm ex}^0 + \mathcal{E}_{\rm d}^0$ is the harmonic part of the energy. It consists of the exchange contribution

$$\mathcal{E}_{\rm ex}^0 = \ell^2 \sum_{\boldsymbol{k}} |\hat{\psi}_{\boldsymbol{k}}|^2 k^2 \tag{12a}$$

and the dipole-dipole contribution

$$\mathcal{E}_{\rm d}^0 = \sum_{\boldsymbol{k}} \left[\frac{g(kh)}{2} - 1\right]|\hat{\psi}_{\boldsymbol{k}}|^2 + \frac{g(kh)}{4}\left[\frac{(k^x - ik^y)^2}{k^2}\hat{\psi}_{\boldsymbol{k}}\hat{\psi}_{-\boldsymbol{k}} + \text{c.c.}\right]. \tag{12b}$$

The nonlinear part of the energy is described by the term $\mathcal{E}^{\rm nl} = \mathcal{E}_{\rm ex}^{\rm nl} + \mathcal{E}_{\rm d}^{\rm nl}$, which consists of nonlinear exchange contribution,

$$\mathcal{E}_{\rm ex}^{\rm nl} = \frac{\ell^2}{4\mathcal{N}_{xy}} \sum_{\boldsymbol{k}_1\boldsymbol{k}_2\boldsymbol{k}_3\boldsymbol{k}_4} [\mathfrak{A}(\boldsymbol{k}_1,\boldsymbol{k}_2)\,\hat{\psi}_{\boldsymbol{k}_1}\hat{\psi}_{\boldsymbol{k}_2}^*\hat{\psi}_{\boldsymbol{k}_3}\hat{\psi}_{\boldsymbol{k}_4}^* \times \Delta(\boldsymbol{k}_1 - \boldsymbol{k}_2 + \boldsymbol{k}_3 - \boldsymbol{k}_4) + \text{c.c.}], \tag{13a}$$

and a dipole-dipole one,

$$\mathcal{E}_{\rm d}^{\rm nl} = -\frac{1}{4\mathcal{N}_{xy}} \sum_{\boldsymbol{k}_1\boldsymbol{k}_2\boldsymbol{k}_3\boldsymbol{k}_4} [\mathfrak{B}(\boldsymbol{k}_1,\boldsymbol{k}_2)\hat{\psi}_{\boldsymbol{k}_1}\hat{\psi}_{\boldsymbol{k}_2}^*\hat{\psi}_{\boldsymbol{k}_3}\hat{\psi}_{\boldsymbol{k}_4}^* \times \Delta(\boldsymbol{k}_1 - \boldsymbol{k}_2 + \boldsymbol{k}_3 - \boldsymbol{k}_4) + \mathfrak{C}(\boldsymbol{k}_1)\hat{\psi}_{\boldsymbol{k}_1}\hat{\psi}_{\boldsymbol{k}_2}^*\hat{\psi}_{\boldsymbol{k}_3}\hat{\psi}_{\boldsymbol{k}_4} \times \Delta(\boldsymbol{k}_1 - \boldsymbol{k}_2 + \boldsymbol{k}_3 + \boldsymbol{k}_4) + \text{c.c.}]. \tag{13b}$$

The characteristic length

$$\ell = \sqrt{\frac{\mathcal{S}^2}{4\pi M_s^2 a^3} \sum_{\boldsymbol{n}} \boldsymbol{n}^2 \mathcal{J}_{\boldsymbol{n}}}, \tag{14}$$

which appears in (12) and (13), is the so-called exchange length. We introduced also the following functions:

$$\mathfrak{A}(\boldsymbol{k}_1,\boldsymbol{k}_2) \equiv k_1^2 - 2(\boldsymbol{k}_1\cdot\boldsymbol{k}_2), \tag{15a}$$

$$\mathfrak{B}(\boldsymbol{k}_1,\boldsymbol{k}_2) \equiv g(|\boldsymbol{k}_1-\boldsymbol{k}_2|h) + \frac{g(k_1 h)}{2} - 1, \tag{15b}$$

$$\mathfrak{C}(\boldsymbol{k}) \equiv g(kh)\frac{(k^x - ik^y)^2}{2k^2}, \tag{15c}$$

$$g(x) \equiv \frac{x + e^{-x} - 1}{x}. \tag{15d}$$

Details describing how to derive the Hamiltonian (11)–(13) in the wave-vector space are in Appendix A.

The function $\mathcal{F}$ represents an action of the spin-polarized current. It consists of two parts,

$$\mathcal{F} = \mathcal{F}^0 + \mathcal{F}^{\rm nl}, \tag{16a}$$

with the harmonic contribution

$$\mathcal{F}^0 = \varkappa \sum_{\boldsymbol{k}} \hat{\psi}^*_{\boldsymbol{k}}\hat{\psi}_{\boldsymbol{k}}, \tag{16b}$$

and the nonlinear part,

$$\mathcal{F}^{\rm nl} = -\frac{\varkappa}{4\Lambda^2\mathcal{N}_{xy}} \sum_{\boldsymbol{k}_1,\boldsymbol{k}_2,\boldsymbol{k}_3,\boldsymbol{k}_4} [\hat{\psi}_{\boldsymbol{k}_1}\hat{\psi}_{\boldsymbol{k}_2}\hat{\psi}^*_{\boldsymbol{k}_3}\hat{\psi}^*_{\boldsymbol{k}_4} \times \Delta(\boldsymbol{k}_1+\boldsymbol{k}_2-\boldsymbol{k}_3-\boldsymbol{k}_4)]. \tag{16c}$$

Note that we are interested in large-scale behavior of the system and restrict our attention to long-wave excitations. Therefore, Eqs. (12), (13), and (15) are written in the limit $ka \ll 1$.

III. HARMONIC APPROXIMATION

First, we discuss the solutions of Eqs. (10) in the harmonic approximation, since they already capture many essential aspects of the problem. By neglecting all nonlinear terms in (10), equations for the complex amplitudes $\hat{\psi}_{\boldsymbol{k}}$ and $\hat{\psi}^*_{-\boldsymbol{k}}$ can be written in the form

$$\begin{aligned} -i\dot{\hat{\psi}}_{\boldsymbol{k}} &= \left[k^2\ell^2 - 1 + \frac{g(hk)}{2} + i\varkappa\right]\hat{\psi}_{\boldsymbol{k}} \\ &\quad + \frac{g(hk)}{2}\frac{(k^x - ik^y)^2}{k^2}\hat{\psi}^*_{-\boldsymbol{k}}, \\ i\dot{\hat{\psi}}^*_{-\boldsymbol{k}} &= \left[k^2\ell^2 - 1 + \frac{g(hk)}{2} - i\varkappa\right]\hat{\psi}^*_{-\boldsymbol{k}} \\ &\quad + \frac{g(hk)}{2}\frac{(k^x + ik^y)^2}{k^2}\hat{\psi}_{\boldsymbol{k}}. \end{aligned} \tag{17}$$

The solutions of Eq. (17) have the form

$$\hat{\psi}_{\boldsymbol{k}}(t) = \Psi_+ e^{z_+(\boldsymbol{k})t}, \qquad \hat{\psi}^*_{-\boldsymbol{k}}(t) = \Psi_- e^{z_-(\boldsymbol{k})t}, \tag{18}$$

where $\Psi_\pm(\boldsymbol{k})$ are time-independent amplitudes and the rate constants $z_\pm(\boldsymbol{k})$ are given by

$$z_\pm(\boldsymbol{k}) = -\varkappa \pm \tilde{\varkappa}(k), \tag{19}$$

where the rate function $\tilde{\varkappa}(k)$ is given by

$$\tilde{\varkappa}(k) = \sqrt{(1-k^2\ell^2)(k^2\ell^2 + g(hk) - 1)}. \tag{20}$$

First, it should be noted that since $\varkappa > 0$, in accordance with (19), the current provides effective damping. That explains why we omitted weak natural damping in Eq. (1). That also explains the previous numerical results, where the saturation and magnetization dynamics under the high spin-current influence were independent of the damping coefficient.[38]

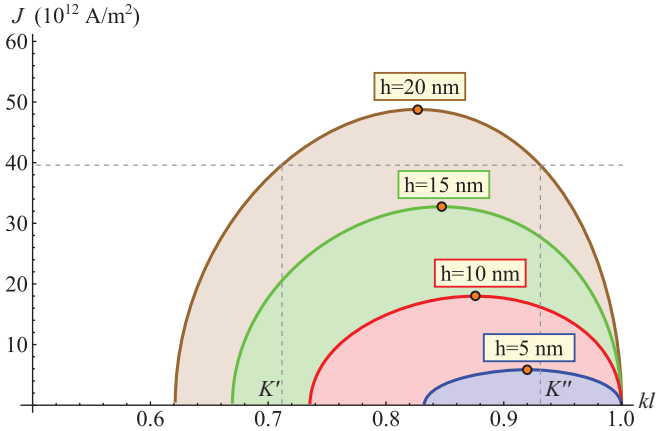

FIG. 1. (Color online) Diagram of stability of the uniform state saturated transversally by spin current. The regions of instability are shown by filling and they are determined by condition $\varkappa < \tilde{\varkappa}$, where the the normalized current $\varkappa$ is rescaled to the real current density J. Thus, for the given current value $J < J_c$, one has the range $[K', K'']$ of the instable wave vectors. The parameters for material and spin current were the same as for the simulations (see Sec. V). Points show the maximums of dependencies $J(k\ell)$ and they determine the saturation current for the given thickness.

Function $\tilde{\varkappa}(k)$ is a nonmonotonic one which reaches its maximum value $\varkappa_c$ at $k = K$,

$$\frac{d\tilde{\varkappa}(K)}{dK} = 0, \quad \varkappa_c = \max_k \tilde{\varkappa}(k) \equiv \tilde{\varkappa}(K)\,. \tag{21}$$

Typical shapes of the rate functions (20) are presented in Fig. 1.

For strong currents, when $\varkappa > \varkappa_c$, we have $\mathrm{Re}\, z_\pm(\boldsymbol{k}) < 0$ for all values of the wave vector $\boldsymbol{k}$. This means that the stationary state of the system is the saturated state with $m_z = 1$. However, for $\varkappa < \varkappa_c$, the saturated state is linearly unstable with respect to modes $\hat{\psi}_{\boldsymbol{k}}$, with wave vectors close to the threshold wave vector K. The corresponding instability domains for different thicknesses are shown in Fig. 1 as filled regions.

For each thickness, the curve $\varkappa = \tilde{\varkappa}(k)$, as well as the corresponding rescaled curve $J(k)$, separates stable and unstable regimes and has a maximum which determines the minimal current J_c, at which the saturated state remains stable. So the critical current at which the transition to saturation occurs can be determined as

$$J_c = \frac{2M_s^2 e}{\eta\hbar} h\varkappa_c. \tag{22}$$

As shown in Fig. 1, the saturation current J_c increases with the increase of thickness. This dependence is presented in detail in Fig. 2.

Using (20) and (22), one can obtain the asymptotic $J_c \approx h^2|e|M_s^2/(2\eta\hbar\ell)$ for $h \ll \ell$ and $J_c \approx h|e|M_s^2/(\eta\hbar)$ for $h \gg \ell$, although the last one is not achieved in Fig. 2 and it is beyond the limits of applicability of the Slonczewski torque in (1). The

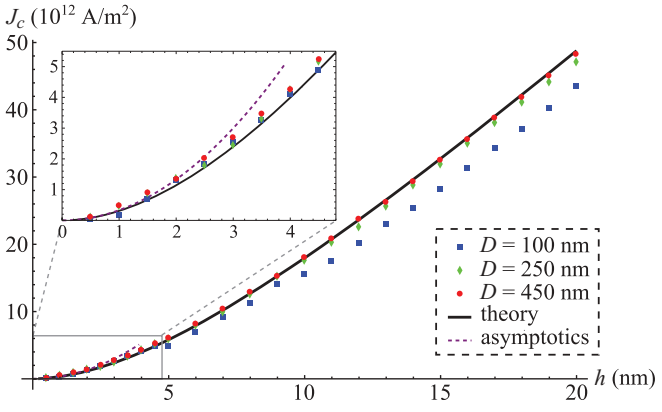

FIG. 2. (Color online) Dependence of the saturation current J_c on the film thickness. The solid line corresponds to the analytical solution obtained from (22) and the results of micromagnetic simulations (see Sec. V) for different disk diameters D are shown by markers. The dashed line demonstrates the parabolic asymptotic for $h \ll \ell$; see text.

critical currents obtained using the micromagnetic simulations appears to be in very good agreement with the theoretical curve. Since the present theory is constructed for a film of infinite lateral size the agreement between simulations and the theory is expectedly the best for samples whose thickness is much smaller than the planar size: $h \ll D$.

IV. WEAKLY NONLINEAR ANALYSIS

In this section, we prove the stability of structures with symmetry C_4 which appear in the presaturation regime. We also show that these stable structures are square vortex-antivortex superlattices. Thus, our analysis is based on Eq. (10) where the nonlinear terms in the Hamiltonian (11) and in the driving function (16) are taken into account.

The simplest way to describe the necessary symmetry is to restrict ourselves only with four wave vectors $\boldsymbol{k} \in \{\boldsymbol{K}_\uparrow, \boldsymbol{K}_\rightarrow, \boldsymbol{K}_\downarrow, \boldsymbol{K}_\leftarrow\}$ in the wave-vector space. Here we use the following notations:

$$\begin{aligned} \boldsymbol{K}_\uparrow &= K(0,1), \quad \boldsymbol{K}_\downarrow = K(0,-1), \\ \boldsymbol{K}_\rightarrow &= K(1,0), \quad \boldsymbol{K}_\leftarrow = K(-1,0), \end{aligned} \tag{23}$$

where the amplitude K is determined for given thickness from the linear analysis as follows: $\varkappa_c = \tilde{\varkappa}(K)$, i.e., K is the wave-vector length which maximizes the dependence $\tilde{\varkappa} = \tilde{\varkappa}(k)$. It should be noted that, since the Hamiltonian $\mathcal{E}$ contains $\hat{\psi}_{\boldsymbol{k}}$ as well as $\hat{\psi}_{-\boldsymbol{k}}$, then our model must contain pairs of vectors $(\boldsymbol{K}, -\boldsymbol{K})$. It means that only structures with even symmetry C_{2n} are possible. We focus here on structures with symmetry C_4 in order to explain the results of the recent numerical experiments.[38]

For future analysis it is convenient to proceed to the following notation:

$$\hat{\psi}_{\boldsymbol{K}_\alpha} \equiv \sqrt{N_\alpha} e^{i\Phi_\alpha}, \tag{24}$$

where $\alpha \in \{\uparrow, \rightarrow, \downarrow, \leftarrow\}$. The value N_α in (24) has the meaning of the number of magnons with the corresponding wave vector. Substituting (24) into the equation of motion (10), we obtain a set of eight equations,

$$\dot{N}_\uparrow = -\frac{\partial \mathcal{E}}{\partial \Phi_\uparrow} - 2\varkappa N_\uparrow \left[1 - \frac{\sum_\alpha N_\alpha - \frac{1}{2}N_\uparrow}{\Lambda^2 \mathcal{N}_{xy}}\right] + \frac{2\varkappa}{\Lambda^2 \mathcal{N}_{xy}} \sqrt{N_\uparrow N_\downarrow N_\rightarrow N_\leftarrow} \cos(\Phi_\updownarrow - \Phi_\leftrightarrow), \tag{25a}$$

$$\dot{\Phi}_\uparrow = \frac{\partial \mathcal{E}}{\partial N_\uparrow} - \frac{\varkappa}{\Lambda^2 \mathcal{N}_{xy}} \frac{\sqrt{N_\downarrow N_\rightarrow N_\leftarrow}}{\sqrt{N_\uparrow}} \sin(\Phi_\updownarrow - \Phi_\leftrightarrow), \tag{25b}$$

where the other three pairs of equations can be obtained by three time-successive rotations of all subscripts by the angle $\pi/2$, and we introduced the notations $\Phi_\updownarrow = \Phi_\uparrow + \Phi_\downarrow$ and $\Phi_\leftrightarrow = \Phi_\rightarrow + \Phi_\leftarrow$ for the sake of simplicity. The Hamiltonian in "$N - \Phi$" notation is presented as a sum of linear and nonlinear parts as follows:

$$\mathcal{E} = \mathcal{E}^0 + \mathcal{E}^{\mathrm{nl}}, \tag{26a}$$

where the linear part reads

$$\mathcal{E}^0 = \left[\ell^2 K^2 - 1 + \frac{g_1}{2}\right](N_\updownarrow + N_\leftrightarrow) - g_1[\sqrt{N_\updownarrow}\cos(\Phi_\updownarrow) - \sqrt{N_\Leftrightarrow}\cos(\Phi_\leftrightarrow)], \tag{26b}$$

and the fourth-order nonlinearity has the following form:

$$\mathcal{E}^{\mathrm{nl}} = \frac{2}{\mathcal{N}_{xy}}\left\{-\frac{1}{4}\left[\ell^2 K^2 - 1 + \frac{g_1}{2}\right]\sum_\alpha N_\alpha^2 + \left[\ell^2 K^2 + 1 - \frac{g_1 + g_2}{2}\right](N_\updownarrow + N_\Leftrightarrow) + 2\left[\ell^2 K^2 + 1 - g_{\sqrt{2}} - \frac{g_1}{2}\right]\sqrt{N_\updownarrow N_\Leftrightarrow} \times \cos(\Phi_\updownarrow - \Phi_\leftrightarrow) + \left[1 - \frac{g_1 + g_{\sqrt{2}}}{2}\right] N_\updownarrow N_\leftrightarrow + \frac{g_1}{4}\left[\sqrt{N_\updownarrow}\left(\frac{3}{2}N_\updownarrow + N_\leftrightarrow\right)\cos\Phi_\updownarrow - \sqrt{N_\Leftrightarrow}\left(\frac{3}{2}N_\leftrightarrow + N_\updownarrow\right)\cos\Phi_\leftrightarrow\right]\right\}. \tag{26c}$$

Here we used the analogous notations $N_\updownarrow = N_\uparrow + N_\downarrow$, $N_\leftrightarrow = N_\rightarrow + N_\leftarrow$, $N_\Updownarrow = N_\uparrow N_\downarrow$, $N_\Leftrightarrow = N_\rightarrow N_\leftarrow$, and $g_\xi \equiv g(\xi Kh)$ to shorten the expressions.

Using (25a) and (26), one can show that

$$\frac{\mathrm{d}}{\mathrm{d}t}(N_\uparrow - N_\downarrow) = -2\varkappa(N_\uparrow - N_\downarrow)\left[1 - \frac{N_\updownarrow + 2N_\leftrightarrow}{2\Lambda^2 \mathcal{N}_{xy}}\right] \tag{27}$$

with the corresponding equation for the subscripts rotated by $\pi/2$. Taking into account that $\varkappa > 0$ we conclude from the Eq. (27) that after period of time $\Delta\tau = 1/(2\varkappa)$ the system achieves a stationary regime with $N_\uparrow = N_\downarrow$ and $N_\rightarrow = N_\leftarrow$. Consideration of these conditions in the stationary form of system (25) leads to the possibility of a solution which satisfies the following conditions:

$$\begin{aligned} &N_\uparrow = N_\downarrow = N_\rightarrow = N_\leftarrow = N, \\ &\Phi_\uparrow + \Phi_\downarrow = \pi + \Phi_\rightarrow + \Phi_\leftarrow = \Phi. \end{aligned} \tag{28}$$

Under condition (28), all four pairs of stationary equations of motion (25) become identical and they obtain the following form:

$$\sin\Phi\left(1-\frac{5}{2}\mathcal{N}\right)g_1 = -2\varkappa\left(1-\frac{5}{2}\frac{\mathcal{N}}{\Lambda^2}\right), \tag{29a}$$

$$\cos\Phi\,(1-5\mathcal{N})\,\frac{g_1}{2} = \ell^2K^2 - 1 + \frac{g_1}{2} - \mathcal{N}\left(\ell^2K^2 - 5 + \frac{5}{2}g_1 + g_2\right), \tag{29b}$$

where $\mathcal{N} = N/\mathcal{N}_{xy}$ is the density of the magnons, and the energy density obtained from the Hamiltonian (26) reads

$$\frac{\mathcal{E}}{\mathcal{N}_{xy}} = 2\mathcal{N}[2(\ell^2K^2-1) + g_1(1-\cos\Phi)] + 2\mathcal{N}^2\left[-\ell^2K^2 + 5 - g_2 - \frac{5}{2}g_1(1-\cos\Phi)\right]. \tag{30}$$

Excluding Φ from (29) and taking into account that $\mathcal{N} \ll 1$, one obtains

$$\mathcal{N} \approx \frac{\varkappa_c^2(h) - \varkappa^2}{\mathfrak{G}\mathfrak{F} + 5\varkappa_c^2\left(1-\frac{1}{\Lambda^2}\right)}, \tag{31a}$$

and then, using (29b), one can estimate

$$\cos\Phi \approx \frac{\mathfrak{F}}{g(Kh)}\sqrt{1 + 4\frac{\mathfrak{G}}{\mathfrak{F}}\mathcal{N}}. \tag{31b}$$

Here we introduced the following thickness-dependent functions $\mathfrak{F} = 2[K^2\ell^2 - 1 + \frac{1}{2}g(Kh)]$ and $\mathfrak{G} = [4K^2\ell^2 - g(2Kh)]$. Magnon density (31a) as well as the corresponding exact solutions of Eqs. (29) are shown in Fig. 3. As one can see, the approximation (31a) is satisfactory near the instability threshold.

Thus, we have proved the possibility of a stationary structure which is described by the four-wave ansatz (23) and (24) in the presaturated regime. At the same time, one can see that the parameter Λ does not influence considerably the system behavior; see the inset in the Fig. 3.

The linear stability analysis for the system (25) shows that the stationary solution (31) is stable in the close vicinity of the critical current

$$0 < \frac{\varkappa_c - \varkappa}{\varkappa_c} \ll 1$$

(see Appendix A for details).

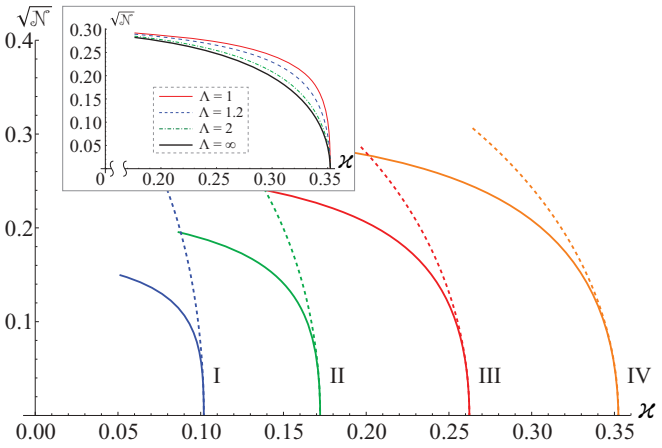

FIG. 3. (Color online) Magnons density as function of the normalized current for different thicknesses (in units of ℓ): I, 0.5; II, 1; III, 2; IV, 4; and $\Lambda = 2$ for all thicknesses. Solid lines show the exact numerical solutions of the system (29) and dashed lines correspond to the approximation (31). (Inset) The weakness of the influence of parameter Λ on the exact solution, and the data correspond to the thickness $h = 4\ell$. Each of the plots is built for the range $[\varkappa_c/2, \varkappa_c]$.

Let us now see how this structure looks. From (8a), one can obtain the following expression for the ψ function:

$$\psi_{\boldsymbol{n}} = \frac{1}{\sqrt{\mathcal{N}_{xy}}}\sum_\alpha \sqrt{N_\alpha}e^{i(\Phi_\alpha + \boldsymbol{K}_\alpha\cdot\boldsymbol{n})}. \tag{32}$$

Varying parameters N_α and Φ_α, one can obtain a wide range of different structures from (32) but under the conditions of (28) the expression (32) results exactly in a square vortex-antivortex superlattice. Indeed, substituting (32) into (6), taking into account the conditions of (28), we obtain, in the linear approximation,

$$\begin{aligned} m_x &\approx 2\sqrt{2\mathcal{N}}\left[\cos(K\bar{x})\sin\frac{\Phi}{2} + \cos(K\bar{y})\cos\frac{\Phi}{2}\right], \\ m_y &\approx 2\sqrt{2\mathcal{N}}\left[\cos(K\bar{x})\cos\frac{\Phi}{2} + \cos(K\bar{y})\sin\frac{\Phi}{2}\right], \\ m_z &\approx 1, \end{aligned} \tag{33}$$

where the following shift of the coordinate origin was performed: $\bar{x} = x + (\Phi_\rightarrow - \Phi_\leftarrow)/(2K)$ and $\bar{y} = y + (\Phi_\uparrow - \Phi_\downarrow)/(2K)$. Magnetization distribution which corresponds to (33) for certain parameters is shown in Fig. 4 by arrows. The topological properties of the system can be characterized by the topological density[42] (or scalar chirality density[37]) $\upsilon = [\partial_x\boldsymbol{m}\times\partial_y\boldsymbol{m}]\cdot\boldsymbol{m}$. The topological density which corresponds to (33) reads

$$\upsilon = -8K^2\mathcal{N}\cos\Phi\sin(K\bar{x})\sin(K\bar{y}). \tag{34}$$

The distribution of (34) is shown in Fig. 4 by gray tones. It resembles chirality waves in Kondo magnets.[37]

Although the model (23) and (24) results in a superlattice that is very similar to the one which is observed in the numerical experiment, one should point out the domain of applicability of this model. In (23) and (24) we use only the critical value of the wave vector K instead of all possible wave vectors in the range $[K', K'']$, where K' and K'' bound the

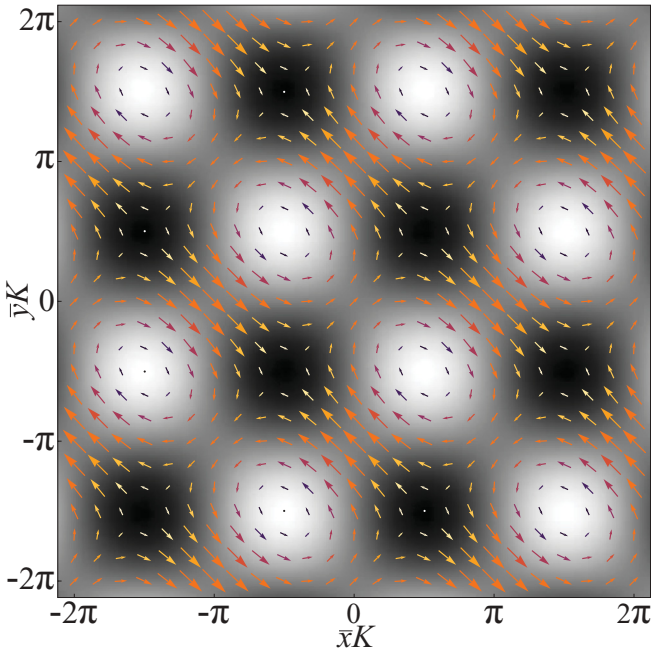

FIG. 4. (Color online) The analytically obtained vortex-antivortex superlattice. Arrows show distribution of magnetization (33) and the corresponding topological density (34) is shown by gray tones. The figure is built for the case $h = 4\ell$ and $\varkappa = 0.65\varkappa_c$ and $\Lambda = 2$ (the required value of Φ was determined from (29) for the noted parameters).

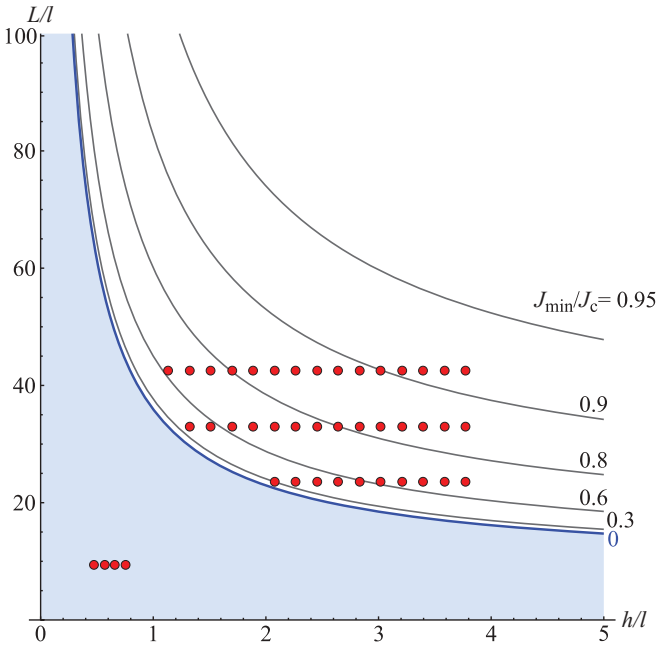

FIG. 5. (Color online) The diagram which determines the range $J \in [J_{\min}, J_c]$ for the given geometry sizes (h, L), where the model (23) and (24) is applicable. In the shaded region the model works for any currents $J < J_c$. Points correspond to the disks, where the superlattices were observed via micromagnetic simulations.

instability domain for the given current value; see Fig. 1. We can restrict ourselves with the single K if the size of the system is small enough,

$$2\pi/L > K'' - K'. \tag{35}$$

Since the domain $\Delta K = K'' - K'$ increases with a decrease in current (see Fig. 1), condition (35) is equivalent to $J_{\min} < J < J_c$, where $J_{\min}$ is the minimal current at which condition (35) exists. For each of the values of thickness h and radius L, one can calculate the value of $J_{\min}$ using (20) and (35); the resulting diagram is shown in Fig. 5. Since, for small thicknesses, $\Delta K \ll 1$, the model (23) and (24) can be used for a wide range of currents.

V. MICROMAGNETIC SIMULATIONS

To investigate numerically the process of magnetic film saturation under the influence of spin-polarized current, we used full-scale OOMMF[43] micromagnetic simulations. All simulations were performed for disk-shaped nanoparticles with material parameters of permalloy as follows: saturation magnetization $M_S = 8.6 \times 10^5$ A/m and exchange constant $A = 13 \times 10^{-12}$ J/m and the anisotropy was neglected. The damping was neglected, because, as shown in Sec. III, the spin-polarized current provides effective damping. The mesh cell was chosen to be $3 \times 3 \times h$ nm. The current parameters $\eta = 0.4$ and $\Lambda = 2$ were the same for all simulations, except for in some cases mentioned in the text below.

In the first stage, we obtained the dependence of saturation current J_c on the sample thickness. For this numerical experiment, we chose nanodisks with three different diameters, $D = 100$, 250, and 450 nm, respectively, and the thickness of each of the particles was varied from 0.5 to 20 nm. Ground state of the particle was used as initial state for the simulations: uniform magnetization within the sample plane for thin disks ($h < 5$ nm) and a vortex state for thicker ones. The spin-current was increased until saturation was achieved. As a criterion of saturation we used the relation $M_z/M_s > 0.9999$, where M_z is the total magnetization along the current direction. The resulting dependence $J_c(h)$ is shown in Fig. 2 by markers. As one can see, for disks with a small aspect ratio, the micromagnetic simulations confirm the analytical results with a high accuracy. The slight deviation from the theoretically predicted curve is observed for the case of small disks (see $D = 100$ nm in the Fig. 2). This is because the presented theory is built for the case of an infinite film that corresponds to a zero aspect ratio.

To study the magnetization dynamics in regime $J \lesssim J_c$ we used a disk with diameter $D = 350$ nm and thickness $h = 20$ nm. A spin current of a certain density was sharply applied to this nanodisk, which initially was in the vortex ground state. After a few nanoseconds, a slowly rotating superlattice was formed for the case where the current value was close to saturation (see Fig. 6) or fluidlike dynamics of the locally ordered vortex-antivortex media was observed for the cases with lower currents (see Fig. 2 in Ref. 38). The Fourier spectrums of the typical crystal and fluid structures are compared in Fig. 7. As shown in Fig. 7(a), the superlattice is square one.

To separate the crystal and fluid phases and to study their properties, we performed a series of simulations for a range

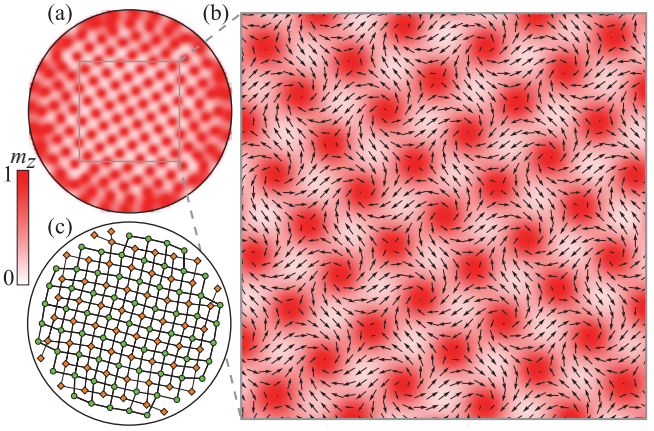

FIG. 6. (Color online) The superlattice structure obtained using simulations in a disk with diameter $D = 350$ nm and thickness $h = 20$ nm under the influence of the current $J = 32 \times 10^{12}$ A/m^2. (a) The out-of-plane structure of the superlattice. (b) Detailed depiction of the magnetization of the central part of the the disk; arrows correspond to the in-plane magnetization distribution and the out-of-plane component m_z is shown by color tone: dark regions correspond to the cores of vortices and antivortices and light regions show the interparticle area. (c) The positions of the vortices and antivortices are shown by disks and rhombuses, respectively.

of currents $J \in [J_c/2,\ J_c]$ with the current step $\Delta J = 0.5 \times 10^{12}$ A/m^2. For a certain value of the current, the magnetization dynamics was simulated for 30 ns. Starting from 2 ns, we saved the magnetization distribution with the time step 0.2 ns. For each of the 0.2-ns magnetization snapshots, we found coordinates of all the particles (vortices and antivortices), using the method[44] of intersection of isolines $m_x = 0$ and $m_y = 0$. To distinguish the vortices from the antivortices, the winding number of each of the particles was calculated as the circulation of a small circumference centered on the particle position. For each of the vortices, the distances to the nearest four antivortices then were found (at this stage, to avoid a boundary influence, we consider only those vortices that were distanced from the disk center by less then half

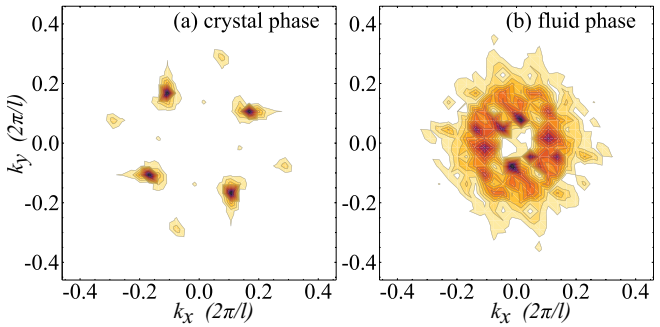

FIG. 7. (Color online) Two-dimensional Fourier spectrums of the crystal (a) and fluid (b) structures. (a) The Fourier transform of the function $m_z(x,y) - \langle m_z \rangle$ for the case of the crystal structure shown in the Fig. 6(b), where $\langle m_z \rangle$ is the averaged m_z component. (b) A fluid structure obtained for current $J = 25 \times 10^{12}$ A/m^2; the other parameters are the same as in Fig. 9.

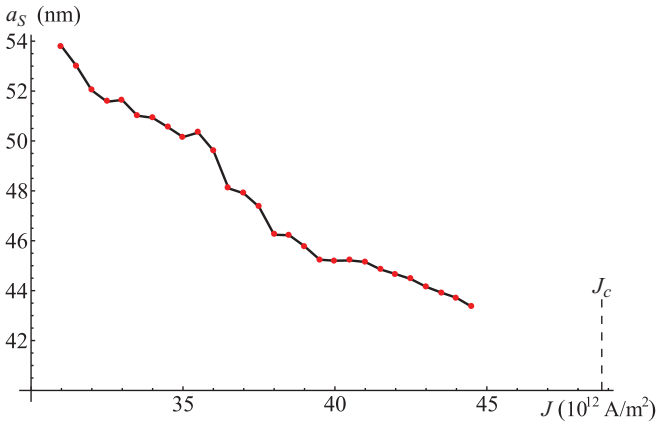

FIG. 8. (Color online) Dependence of the superlattice constant a_S on the applied current for permalloy disk with diameter $D = 350$ nm and thickness 20 nm. Data were obtained using micromagnetic simulations.

of the disk radius). The histogram of the distribution of all obtained vortex-antivortex distances then was built for a certain magnetization snapshot, and, finally, we built the averaged histogram based on all magnetization snapshots for a certain current value. Two examples of these averaged histograms are shown in the left column of Fig. 9. The obtained histograms can be well fitted by the Gaussian $f(x) \propto \exp[-(x - x_0)^2/\sigma^2]$, where $f(x)$ is number of the vortex-antivortex distances which are in the interval $[x,\ x + \Delta x]$, with $\Delta x = 1$ nm being the width of the histogram bin.

For the crystal phase, the superlattice constant was considered to be $a_s = 2x_0$. We found that the superlattice constant slightly decreases with the increase of current; this dependence

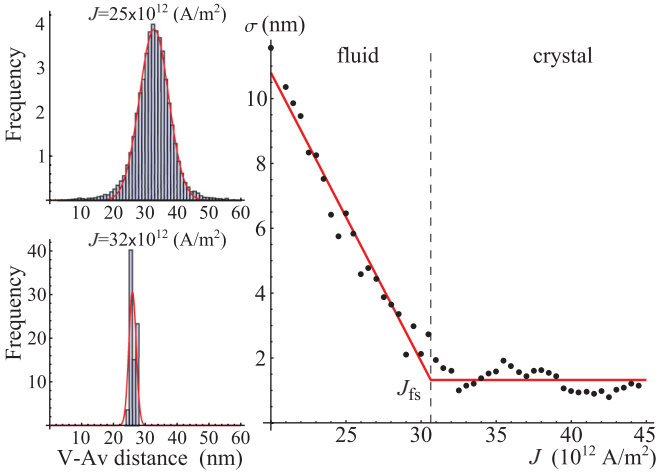

FIG. 9. (Color online) The criterium of separation of fluid and crystal phases. In the left column, the distributions of the distances between the nearest vortices and antivortices are presented; the solid line shows the Gaussian approximation. The upper and lower histograms correspond to the typical fluidlike and crystallike structures, respectively. The right plot demonstrates dependence of the half-width of the mentioned distributions on the applied current. All data are obtained from simulations for disk with $D = 350$ nm, $h = 20$ nm, and $\Lambda = 2$.

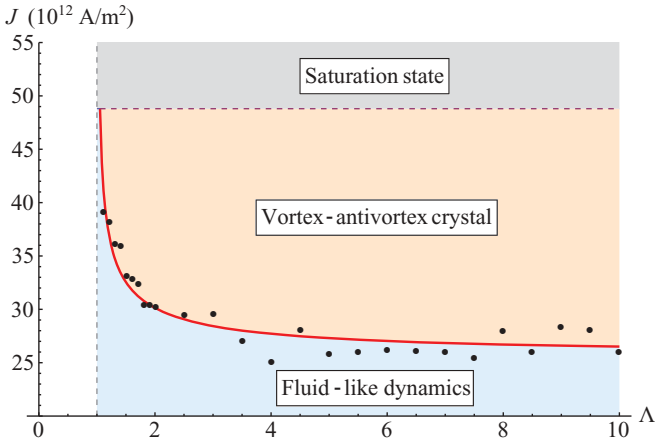

FIG. 10. (Color online) Phase diagram of the presaturated magnetic film with thickness $h = 20$ nm. The transition current J_{fc}, obtained from the simulation data (see Sec. V and Fig. 9), is shown by points and the corresponding fitting (36) is shown by the solid line.

is shown in Fig. 8. However, we were not able to determine a_s close to the saturation current because the components of magnetization, m_x and m_y, become vanishingly small. The obtained dependence $a_s(J)$ appears to be not very smooth because of the stress in the superlattice due to presence of the boundary.

An important characteristic which can be extracted from histograms is the $\sigma(J)$ dependence. It gives a possibility quantitatively separates fluid phase and crystal one: In crystals, the value of σ is small (about a few nanometers) and is weakly dependent on the current J; in the fluid phase, the value of σ increases fast with the decrease of current. To determine the critical current J_{fc} of the transition between the fluid and crystal phases, we fit the numerically obtained dependence $\sigma(J)$ by the function $\sigma = (aJ + b)\theta(-J + J_{fc}) + (aJ_{fc} + b)\theta(J - J_{fc})$, with $\theta(x)$ being the Heaviside step function and a and b being the fitting parameters (see Fig. 9).

According to the linear analysis (Sec. III), the parameter Λ does not influence the saturation current J_c, and, according to the weakly nonlinear analysis of the presaturated regime (Sec. IV), the parameter Λ influences very weakly on the dynamics of the vortex-antivortex superlattice. Our theory is not able to describe the transition between the fluid and crystal phases, but, using the simulations and the methods described above, we found that the current J_{fc} and, consequently, the current range $[J_{fc}, J_c]$ of the crystal phase existence depend on parameter Λ (see the Fig. 10). We found that $J_{fc}(\Lambda)$ dependence can be well fitted by the function

$$J_{fc} = \frac{\beta}{\sqrt{\Lambda^2 - 1}} + J_{fc}^0, \tag{36}$$

with $\beta \approx 7.78 \times 10^{12}$ A/m^2 and $J_{fc}^0 \approx 25.92 \times 10^{12}$ A/m^2 being the critical current of the phase transition for case $\Lambda \to \infty$. For the case $\Lambda = 1$ the superlattice is not formed, only the fluid-like dynamics is observed. Moreover, the current region of the crystal phase quickly shortens when the parameter Λ is reduced to 1, but, for $\Lambda > 4$, the the crystal region is approximately constant. It should be stressed that we do not consider here the "gas" phase and the rarefied patterns which were observed in Ref. 38 at lower currents $J \ll J_c$.

It is important to note that the current density required for the pattern formation is high. This is why Joule heating of the sample can be essential. Thermal effects during large current density applied to the nanowires were reported for domain wall motion:[45,46] The rise in temperature estimated from the resistance increase does not affect the magnetization process. Influence of the temperature was found to be nonessential for current-induced vortex nucleation and annihilation in the vortex domain walls[47] and for the current-induced motion of individual vortex in Py nanodisks.[48] While magnetic vortices are stable up to very high temperatures,[49] the heating can influence the typical magnetization reversal parameters. In particular, there exists the temperature dependence of the critical fields for vortex nucleation and annihilation.[50] In order to estimate the influence of temperature on the process of vortex-antivortex pattern formation, we model the thermal effects by including the noise field in the Landau-Lifshitz-Slonczewski equation (1) in the same way as was used to study the switching phenomena in Ref. 51. We used a disk with diameter $D = 350$ nm and thickness $h = 20$ nm with noise fields of different intensities. We found that the vortex crystal formed by current $J = 36 \times 10^{12}$ A/m^2 is stable up to the field intensity of about 0.5 T, with $\Delta t = 1$ ps being the the characteristic time of the noise field variation. These simulations demonstrate the stability of the vortex-antivortex lattice with respect to the random noise. It is worth noting that the relationship between the noise field and the temperature in the presence of the spin-polarized current is an open question and it is beyond the scope of the current paper.[52]

VI. CONCLUSIONS

We studied theoretically the process of vortex-antivortex pattern formation in thin ferromagnetic films under the action of a strong transversally spin-polarized current. We show that there exists a critical (or saturation) current J_c above which the film goes to a saturated state with all magnetic moments directed perpendicularly to the film plane. The critical current strongly depends on the sample thickness and it is practically independent of the lateral size of the magnet. The saturation current increases with increasing thickness, following the squared law for thin samples and a linear one for thick samples. We demonstrate that the stable regular structures with symmetry C_4 can appear in the presaturated regime and we show that these structures are square vortex-antivortex superlattices. The spatial period of the superlattice slightly decreases with an increase of current. The micromagnetic simulations confirm our analytical results with a high accuracy. Using the simulations, we describe the melting of the vortex crystal with the current decrease.

We show that parameter Λ, which controls the spin-transfer torque efficiency, does not modify significantly either the saturation current J_c or the dynamics of the vortex-antivortex superlattice. In contrast to this, the critical current J_{fc}, which gives the boundary between the fluid phase and the crystal one, is very sensitive to the spin-torque efficiency parameter Λ: The

interval of the crystal phase existence $[J_{fc}, J_c]$ contracts when $\Lambda \to 1$ and it is constant for $\Lambda \gg 1$.

APPENDIX A: HAMILTONIAN IN THE RECIPROCAL SPACE

Here we calculate the magnetic energy in the wave-vector space, limiting ourselves to fourth-order nonlinearity.

1. Exchange energy

Let us consider, first, the exchange energy. Substituting the magnetization (6) written in terms of ψ into the general expression (2), one can write the total exchange energy in the form $E_{ex} \approx E^0_{ex} + E^{nl}_{ex}$, where the linear part reads

$$E^0_{ex} = -\mathcal{S}^2\mathcal{N}_z \sum_{\boldsymbol{n},\boldsymbol{l}\neq\boldsymbol{0}} \mathcal{J}_{\boldsymbol{l}}\left[\psi_{\boldsymbol{n}}\psi^*_{\boldsymbol{n}+\boldsymbol{l}} - \frac{1}{2}(|\psi_{\boldsymbol{n}}|^2 + |\psi_{\boldsymbol{n}+\boldsymbol{l}}|^2) + \text{c.c.}\right]$$

and the corresponding nonlinear part takes the form

$$E^{nl}_{ex} = -\frac{\mathcal{S}^2\mathcal{N}_z}{4} \sum_{\boldsymbol{n},\boldsymbol{l}\neq\boldsymbol{0}} \mathcal{J}_{\boldsymbol{l}}[\psi_{\boldsymbol{n}}\psi^*_{\boldsymbol{n}+\boldsymbol{l}}(|\psi_{\boldsymbol{n}}|^2 + |\psi_{\boldsymbol{n}+\boldsymbol{l}}|^2) - 2|\psi_{\boldsymbol{n}}|^2|\psi_{\boldsymbol{n}+\boldsymbol{l}}|^2 + \text{c.c.}].$$

Let us perform the Fourier transform (8a) taking into account the orthogonality condition (9), which results in

$$E^0_{ex} = 2\mathcal{S}^2\mathcal{N}_z \sum_{\boldsymbol{l}} \mathcal{J}_{\boldsymbol{l}} \sum_{\boldsymbol{k}} |\hat{\psi}_{\boldsymbol{k}}|^2(1 - e^{i\boldsymbol{k}\cdot\boldsymbol{l}}),$$

$$E^{nl}_{ex} = \frac{\mathcal{S}^2\mathcal{N}_z}{4\mathcal{N}_{xy}} \sum_{\boldsymbol{l}} \mathcal{J}_{\boldsymbol{l}} \sum_{\boldsymbol{k}_1\boldsymbol{k}_2\boldsymbol{k}_3\boldsymbol{k}_4} [\hat{\psi}_{\boldsymbol{k}_1}\hat{\psi}^*_{\boldsymbol{k}_2}\hat{\psi}_{\boldsymbol{k}_3}\hat{\psi}^*_{\boldsymbol{k}_4} e^{i(\boldsymbol{k}_3-\boldsymbol{k}_4)\boldsymbol{l}} \times (e^{-i\boldsymbol{k}_2\boldsymbol{l}} + e^{i\boldsymbol{k}_4\boldsymbol{l}} - 2)\Delta(\boldsymbol{k}_1 - \boldsymbol{k}_2 + \boldsymbol{k}_3 - \boldsymbol{k}_4) + \text{c.c.}].$$

We now use the assumption that the magnons whose wavelength is of the same order with a are not essential for the considered phenomenon; in other words, we assume that $ak \ll 1$. In this case, we can expand the exponents in the exchange energy into a series on ak, and then, performing the normalization, we finally obtain the expressions (12a) and (13a) for the exchange energy.

2. Dipole-dipole energy

In case of the dipole-dipole energy, we start from the general expression (3). Taking into account that the magnetization is uniform along the z coordinate, one can write the energy (3) in the form[53]

$$E_d = -\frac{M_s^2a^6}{2} \sum_{\boldsymbol{n},\boldsymbol{l}} \left[A_{\boldsymbol{nl}}\left(\boldsymbol{m}_{\boldsymbol{n}}\boldsymbol{m}_{\boldsymbol{l}} - 3m^z_{\boldsymbol{n}}m^z_{\boldsymbol{l}}\right) + B_{\boldsymbol{nl}}\left(m^x_{\boldsymbol{n}}m^x_{\boldsymbol{l}} - m^y_{\boldsymbol{n}}m^y_{\boldsymbol{l}}\right) + C_{\boldsymbol{nl}}\left(m^x_{\boldsymbol{n}}m^y_{\boldsymbol{l}} + m^y_{\boldsymbol{n}}m^x_{\boldsymbol{l}}\right)\right],$$

where the coefficients A, B, and C are as follows:

$$A_{\boldsymbol{nl}} = \frac{1}{2} \sum_{\substack{\nu_z,\lambda_z \\ \boldsymbol{\nu}\neq\boldsymbol{\lambda}}} \frac{(\lambda_x - \nu_x)^2 + (\lambda_y - \nu_y)^2 - 2(\lambda_z - \nu_z)^2}{|\boldsymbol{\lambda} - \boldsymbol{\nu}|^5},$$

$$B_{\boldsymbol{nl}} = \frac{3}{2} \sum_{\substack{\nu_z,\lambda_z, \\ \boldsymbol{\nu}\neq\boldsymbol{\lambda}}} \frac{(\lambda_x - \nu_x)^2 - (\lambda_y - \nu_y)^2}{|\boldsymbol{\lambda} - \boldsymbol{\nu}|^5},$$

$$C_{\boldsymbol{nl}} = 3 \sum_{\substack{\nu_z,\lambda_z \\ \boldsymbol{\nu}\neq\boldsymbol{\lambda}}} \frac{(\lambda_x - \nu_x)(\lambda_y - \nu_y)}{|\boldsymbol{\lambda} - \boldsymbol{\nu}|^5}.$$

Here $\boldsymbol{\nu} = (\nu_x, \nu_y, \nu_z)$ and $\boldsymbol{\lambda} = (\lambda_x, \lambda_y, \lambda_z)$ are three-dimensional indexes while $\boldsymbol{n} = (\nu_x, \nu_y)$ and $\boldsymbol{l} = (\lambda_x, \lambda_y)$ are the corresponding two-dimensional ones. Substituting (6) into the dipolar energy and taking into account that $A_{\boldsymbol{nl}} = A_{\boldsymbol{ln}}$, $B_{\boldsymbol{nl}} = B_{\boldsymbol{ln}}$, and $C_{\boldsymbol{nl}} = C_{\boldsymbol{ln}}$, one obtains the following expression for dipole-dipole energy $E_d = E^0_d + E^{nl}_d$, where

$$E^0_d = -\frac{M_s^2a^6}{2} \sum_{\boldsymbol{n},\boldsymbol{l}} [A_{\boldsymbol{nl}}(2|\psi_{\boldsymbol{n}}|^2 + \psi_{\boldsymbol{n}}\psi^*_{\boldsymbol{l}}) + D_{\boldsymbol{nl}}\psi_{\boldsymbol{n}}\psi_{\boldsymbol{l}} + \text{c.c.}], \tag{A1a}$$

$$E^{nl}_d = \frac{M_s^2a^6}{2} \sum_{\boldsymbol{n},\boldsymbol{l}} \left[A_{\boldsymbol{nl}}|\psi_{\boldsymbol{n}}|^2\left(|\psi_{\boldsymbol{l}}|^2 + \frac{1}{2}\psi_{\boldsymbol{n}}\psi^*_{\boldsymbol{l}}\right) + \frac{1}{2}D_{\boldsymbol{nl}}|\psi_{\boldsymbol{n}}|^2\psi_{\boldsymbol{n}}\psi_{\boldsymbol{l}} + \text{c.c.}\right]. \tag{A1b}$$

Here the notation $D_{\boldsymbol{nl}} = B_{\boldsymbol{nl}} - iC_{\boldsymbol{nl}}$ was introduced. Now we substitute (8a) into (A1) and perform the summation over $\boldsymbol{n}$ with taking into account (9) and, finally, we obtain

$$E^0_d = -\frac{M_s^2a^6}{2} \sum_{\boldsymbol{k}} \{|\hat{\psi}_{\boldsymbol{k}}|^2[2\hat{A}(0) + \hat{A}(\boldsymbol{k})] + \hat{D}(\boldsymbol{k})\hat{\psi}_{\boldsymbol{k}}\hat{\psi}_{-\boldsymbol{k}} + \text{c.c.}\}, \tag{A2a}$$

$$E^{nl}_d = \frac{M_s^2a^6}{4\mathcal{N}_{xy}} \sum_{\boldsymbol{k}_1\boldsymbol{k}_2\boldsymbol{k}_3\boldsymbol{k}_4} \{[2\hat{A}(\boldsymbol{k}_1 - \boldsymbol{k}_2) + \hat{A}(\boldsymbol{k}_1)] \times \hat{\psi}_{\boldsymbol{k}_1}\hat{\psi}^*_{\boldsymbol{k}_2}\hat{\psi}_{\boldsymbol{k}_3}\hat{\psi}^*_{\boldsymbol{k}_4}\Delta(\boldsymbol{k}_1 - \boldsymbol{k}_2 + \boldsymbol{k}_3 - \boldsymbol{k}_4) + \hat{D}(\boldsymbol{k}_1)\hat{\psi}_{\boldsymbol{k}_1}\hat{\psi}^*_{\boldsymbol{k}_2}\hat{\psi}_{\boldsymbol{k}_3}\hat{\psi}_{\boldsymbol{k}_4}\Delta(\boldsymbol{k}_1 - \boldsymbol{k}_2 + \boldsymbol{k}_3 + \boldsymbol{k}_4) + \text{c.c.}\}. \tag{A2b}$$

where functions $\hat{A}(\boldsymbol{k})$ and $\hat{D}(\boldsymbol{k})$ are determined as follows:

$$\hat{A}(\boldsymbol{k}) = \frac{1}{2} \sum_{\boldsymbol{l}} \sum_{\nu_z,\lambda_z} \frac{x_{\boldsymbol{l}}^2 + y_{\boldsymbol{l}}^2 - 2(z_{\nu_z} - z_{\lambda_z})^2}{\left[x_{\boldsymbol{l}}^2 + y_{\boldsymbol{l}}^2 + (z_{\nu_z} - z_{\lambda_z})^2\right]^{5/2}} e^{i\boldsymbol{l}\boldsymbol{k}}, \tag{A3a}$$

$$\hat{D}(\boldsymbol{k}) = \frac{3}{2} \sum_{\boldsymbol{l}} \sum_{\nu_z,\lambda_z} \frac{x_{\boldsymbol{l}}^2 - y_{\boldsymbol{l}}^2 - 2ix_{\boldsymbol{l}}y_{\boldsymbol{l}}}{\left[x_{\boldsymbol{l}}^2 + y_{\boldsymbol{l}}^2 + (z_{\nu_z} - z_{\lambda_z})^2\right]^{5/2}} e^{i\boldsymbol{l}\boldsymbol{k}}. \tag{A3b}$$

The form of the functions $\hat{A}(\boldsymbol{k})$ and $\hat{D}(\boldsymbol{k})$ is not convenient for an analysis, therefore, we perform an approximate transition from summation to integration in (A3). Let us start from the function $\hat{A}(\boldsymbol{k})$,

$$\hat{A}(\boldsymbol{k}) = \frac{1}{a^4} \lim_{r_0\to 0} \int_{w(r_0)} \mathrm{d}^3\boldsymbol{r}(h - z)\frac{x^2 + y^2 - 2z^2}{[x^2 + y^2 + z^2]^{5/2}} e^{i(xk^x + yk^y)}, \tag{A4}$$

where we picked out the coordinate origin from the domain of integration $\omega(r_0)$ (see the Fig. 11) and we also used the relation

$$\int_0^h dz \int_0^h dz' F(|z - z'|) = 2\int_0^h (h - z)F(z)dz. \tag{A5}$$

Separating the region of integration $\omega(r_0)$ into parts I and II (see Fig. 11) and performing the change of variables $(x, y) = \rho(\cos\chi, \sin\chi)$, we can represent the function $\hat{A}$ as a sum,

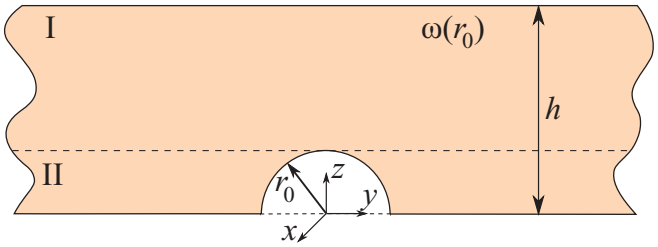

FIG. 11. (Color online) Cross section of the film. The filling shows domain of integration $\omega(r_0)$ used in the calculation of function $\hat{A}(\boldsymbol{k})$ in (A4).

$\hat{A}(\boldsymbol{k}) = (A_I + A_{II})/a^4$, where

$$\frac{A_{\rm I}}{2\pi} = \lim_{\rho_0\to 0}\int_{\rho_0}^{h} dz(h-z)\int_0^{\infty} d\rho\rho\,\frac{\rho^2-2z^2}{[\rho^2+z^2]^{5/2}}J_0(\rho k), \tag{A6a}$$

$$\frac{A_{\rm II}}{2\pi} = \lim_{\rho_0\to 0}\int_0^{\rho_0} dz(h-z\int_{\sqrt{\rho_0^2-z^2}}^{\infty} d\rho\rho\,\frac{\rho^2-2z^2}{[\rho^2+z^2]^{5/2}}J_0(\rho k). \tag{A6b}$$

Here we performed integration over $\chi \in [0, 2\pi]$ using the relation $\int_0^{2\pi} e^{i\rho(k^x\cos\chi + k^y\sin\chi)}d\chi = 2\pi J_0(k\rho)$, where $J_0(x)$ denotes a zero-order Bessel function of the first kind. Direct integration in (A6a) with the consequent limit calculation results $A_{\rm I}/2\pi = -hg(kh)$, where $g(x) = (e^x + x - 1)/x$. Change of variables $\rho \to \rho_0\rho$ and $z \to \rho_0 z$ allows us to get rid of the ρ_0 in the integration limits,

$$\frac{A_{\rm II}}{2\pi} = \lim_{\rho_0\to 0}\int_0^{1} dz(h-z\rho_0)\int_{\sqrt{1-z^2}}^{\infty} d\rho\rho\,\frac{\rho^2-2z^2}{[\rho^2+z^2]^{5/2}}J_0(\rho\rho_0 k). \tag{A7}$$

We then calculate the limit in (A7) with the subsequent integration results $A_{\rm II}/2\pi = h2/3$, so, finally,

$$\hat{A}(\boldsymbol{k}) = \frac{2\pi h}{a^4}\left[\frac{2}{3} - g(kh)\right]. \tag{A8}$$

Performing the same transition to the polar coordinates (ρ, χ), we represent (A3b) as follows:

$$\hat{D}(\boldsymbol{k}) = \frac{1}{a^4}\int_0^{h} dz(h-z)\int_0^{\infty}\frac{\rho^3 d\rho}{[\rho^2+z^2]^{5/2}}\int_0^{2\pi} d\chi\, e^{-i(\boldsymbol{\rho k}+2\chi)}, \tag{A9}$$

where $\boldsymbol{\rho k} = \rho(k^x\cos\chi + k^y\sin\chi)$. The direct integration (A9) using the relation $\int_0^{2\pi} d\chi e^{i(x\cos\chi + n\chi)} = 2\pi i^n J_n(x)$ results in

$$\hat{D}(\boldsymbol{k}) = -\frac{2\pi h}{a^4}g(kh)\frac{(k^x - ik^y)^2}{k^2}. \tag{A10}$$

Substituting now (A8) and (A10) into (A 2), we obtain the expressions (12b) and (13b) for the dipole-dipole energy.

APPENDIX B: STABILITY OF THE VORTEX-ANTIVORTEX LATTICE SOLUTION

Here we consider the stability of the stationary solution (28) and (31) of the system (25). As shown in the main text, after a period of time $\tau = 1/(2\varkappa)$, the solutions of Eqs. (25) satisfy the conditions $N_\uparrow = N_\downarrow$ and $N_\rightarrow = N_\leftarrow$. Using these conditions and introducing the variables $N_1 = N_\uparrow = N_\downarrow$, $N_2 = N_\rightarrow = N_\leftarrow$, $\Phi_1 = \Phi_\uparrow + \Phi_\downarrow$, and $\Phi_2 = \Phi_\rightarrow + \Phi_\leftarrow$, one can reduce the system of eight equations (25) to a system of four equations,

$$\begin{aligned}\dot{N}_i &= -\frac{\partial\mathcal{E}}{\partial\Phi_i} - F_i^N,\\ \dot{\Phi}_i &= \frac{\partial\mathcal{E}}{\partial N_i} - F_i^\Phi, \qquad i = 1,2.\end{aligned} \tag{B1}$$

Here the forces of the acting spin-current has the form

$$\begin{aligned}F_i^N &= 2\varkappa\left\{N_i\left[1 - \frac{3N_i + 4N_{\bar{i}}}{2\Lambda^2\mathcal{N}_{xy}}\right] - \frac{N_i N_{\bar{i}}}{\Lambda^2\mathcal{N}_{xy}}\cos(\Phi_i - \Phi_{\bar{i}})\right\},\\ F_i^\Phi &= \frac{2\varkappa}{\Lambda^2\mathcal{N}_{xy}}N_{\bar{i}}\sin(\Phi_i - \Phi_{\bar{i}}),\end{aligned} \tag{B2}$$

where the notation $\bar{1} = 2$ and $\bar{2} = 1$ is used. Hamiltonian (26) in terms of the new variables takes the form

$$\mathcal{E} = \mathcal{E}^0 + \mathcal{E}^{\rm nl}, \tag{B3a}$$

where the linear part (26b) reads

$$\begin{aligned}\mathcal{E}^0 = 2(N_1 + N_2)&\left(K^2\ell^2 + \frac{g_1}{2} - 1\right)\\ &- g_1(N_1\cos\Phi_1 - N_2\cos\Phi_2)\end{aligned} \tag{B3b}$$

and the corresponding nonlinear part (26c) is

$$\begin{aligned}\mathcal{E}^{\rm nl} = \frac{1}{\mathcal{N}_{xy}}\Bigg(\sum_{i=1,2}\Bigg\{&N_i^2\left(3 + K^2\ell^2 - \frac{3}{2}g_1 - g_2\right)\\ &+ 2N_iN_{\bar{i}}\Bigg[\cos(\Phi_i - \Phi_{\bar{i}})\left(1 + K^2\ell^2 - \frac{g_1}{2} - g_{\sqrt{2}}\right)\\ &+ 2 - g_1 - g_{\sqrt{2}}\Bigg]\Bigg\} + \frac{3}{2}g_1\left(N_1^2\cos\Phi_1 - N_2^2\cos\Phi_2\right)\\ &+ g_1N_1N_2(\cos\Phi_1 - \cos\Phi_2)\Bigg).\end{aligned} \tag{B3c}$$

Now we linearize the system (B1) against a stationary solution $\mathbf{v}^0 = \{N_1^0, N_2^0, \Phi_1^0, \Phi_2^0\}$:

$$\dot{\tilde{\mathbf{v}}} = \mathbf{M}\tilde{\mathbf{v}}, \tag{B4}$$

where $\tilde{\boldsymbol{v}}$ is small deviation from the solution $\mathbf{v}^0$ and 4×4 matrix $\mathbf{M}$ can be presented in the following block form:

$$\mathbf{M} = \begin{pmatrix}\mathbf{M}^{NN} & \mathbf{M}^{N\Phi}\\ \mathbf{M}^{\Phi N} & \mathbf{M}^{\Phi\Phi}\end{pmatrix}_{\mathbf{v}=\mathbf{v}^0}, \tag{B5a}$$

where the components are the following 2×2 matrices:

$$\begin{aligned}\mathbf{M}_{i,j}^{NN} &= -\frac{\partial^2\mathcal{E}}{\partial N_i\partial N_j} - \frac{\partial F_i^N}{\partial N_j},\\ \mathbf{M}_{i,j}^{N\Phi} &= -\frac{\partial^2\mathcal{E}}{\partial N_i\partial\Phi_j} - \frac{\partial F_i^N}{\partial\Phi_j},\\ \mathbf{M}_{i,j}^{\Phi N} &= \frac{\partial^2\mathcal{E}}{\partial\Phi_i\partial N_j} - \frac{\partial F_i^\Phi}{\partial N_j},\\ \mathbf{M}_{i,j}^{\Phi\Phi} &= \frac{\partial^2\mathcal{E}}{\partial\Phi_i\partial\Phi_j} - \frac{\partial F_i^\Phi}{\partial\Phi_j}, \quad i,j = 1,2.\end{aligned} \tag{B5b}$$

A necessary and sufficient condition for the stability of the solution $\mathbf{v}^0$ is negativity of the real parts of all eigenvalues $\lambda_1, \lambda_2, \lambda_3, \lambda_4$ of the matrix $\mathbf{M}$. After the straightforward calculation of (B5b) we substitute the solution $N_1 = N_2 = N$, $\Phi_1 = \Phi$, and $\Phi_2 = \Phi - \pi$, which corresponds to the conditions (28). Then, after the straightforward calculation of the eigenvalues of $\mathbf{M}$, we exclude Φ using (29) and, finally, we obtain

$$\begin{aligned}
\lambda_1 &= -\varkappa - \sqrt{2\varkappa_c^2 - \varkappa^2} + \frac{2\mathscr{N}}{\varkappa_c}\left[\mathfrak{FG} + \varkappa_c^2\left(3 + \frac{1}{\Lambda^2}\right)\right],\\
\lambda_2 &= -\varkappa + \sqrt{2\varkappa_c^2 - \varkappa^2} - \frac{2\mathscr{N}}{\varkappa_c}\left[\mathfrak{FG} + 3\varkappa_c^2\left(1 - \frac{1}{\Lambda^2}\right)\right],\\
\lambda_3 &= -\varkappa + \sqrt{2\varkappa_c^2 - \varkappa^2} - \frac{2\mathscr{N}}{\varkappa_c}\left[\mathfrak{FG} + 5\varkappa_c^2\left(1 - \frac{1}{\Lambda^2}\right)\right],\\
\lambda_4 &= -\varkappa - \sqrt{2\varkappa_c^2 - \varkappa^2} + \frac{2\mathscr{N}}{\varkappa_c}\left[\mathfrak{FG} + 5\varkappa_c^2\right],
\end{aligned} \tag{B6}$$

where only the terms linear with respect to $\mathscr{N}$ are saved. It should be noted that for $\mathscr{N} = 0$ (what corresponds to the saturated state) the condition $\lambda_i < 0$ in (B6) is equivalent to the condition of stability of the saturated state $\varkappa > \varkappa_c$. Substituting (31a) into (B6) and considering the indefinitely small deviation from the saturation current $\varkappa = \varkappa_c + \delta$, one obtains the following linear approximation of (B6) with respect to deviation δ:

$$\begin{aligned}
\lambda_1 &= -2\left[\varkappa_c + 2\delta\frac{\mathfrak{FG} + \varkappa_c^2\left(3 + \frac{1}{\Lambda^2}\right)}{\mathfrak{FG} + 5\varkappa_c^2\left(1 - \frac{1}{\Lambda^2}\right)}\right],\\
\lambda_2 &= 4\delta\left[\frac{\mathfrak{FG} + 3\varkappa_c^2\left(1 - \frac{1}{\Lambda^2}\right)}{\mathfrak{FG} + 5\varkappa_c^2\left(1 - \frac{1}{\Lambda^2}\right)} - \frac{1}{2}\right],\\
\lambda_3 &= 2\delta,\\
\lambda_4 &= -2\left[\varkappa_c + 2\delta\frac{\mathfrak{FG} + 5\varkappa_c^2}{\mathfrak{FG} + 5\varkappa_c^2\left(1 - \frac{1}{\Lambda^2}\right)}\right].
\end{aligned} \tag{B7}$$

Taking into account that $\mathfrak{FG} > 0$ and $\Lambda > 1$, one can conclude that all $\lambda_i < 0$ only for $\delta < 0$. This means that the obtained lattice solution (28) and (31) is stable for an infinitely small decrease in current from the critical value.

*sheka@univ.net.ua

[1] J. Lindner, Superlattices Microstruct. **47**, 497 (2010).
[2] S. Bohlens, B. Krüger, A. Drews, M. Bolte, G. Meier, and D. Pfannkuche, Appl. Phys. Lett. **93**, 142508 (2008).
[3] A. Drews, B. Kruger, G. Meier, S. Bohlens, L. Bocklage, T. Matsuyama, and M. Bolte, Appl. Phys. Lett. **94**, 062504 (2009).
[4] E. B. Myers, D. C. Ralph, J. A. Katine, R. N. Louie, and R. A. Buhrman, Science **285**, 867 (1999).
[5] J. A. Katine, F. J. Albert, R. A. Buhrman, E. B. Myers, and D. C. Ralph, Phys. Rev. Lett. **84**, 3149 (2000).
[6] E. B. Myers, F. J. Albert, J. C. Sankey, E. Bonet, R. A. Buhrman, and D. C. Ralph, Phys. Rev. Lett. **89**, 196801 (2002).
[7] S. I. Kiselev, J. C. Sankey, I. N. Krivorotov, N. C. Emley, R. J. Schoelkopf, R. A. Buhrman, and D. C. Ralph, Nature **425**, 380 (2003).
[8] Z. Li and S. Zhang, Phys. Rev. Lett. **92**, 207203 (2004).
[9] M. Maicas, Physica B: Condensed Matter **343**, 247 (2004).
[10] J.-G. Caputo, Y. Gaididei, F. G. Mertens, and D. D. Sheka, Phys. Rev. Lett. **98**, 056604 (2007).
[11] B. A. Ivanov and C. E. Zaspel, Phys. Rev. Lett. **99**, 247208 (2007).
[12] D. D. Sheka, Y. Gaididei, and F. G. Mertens, Appl. Phys. Lett. **91**, 082509 (2007).
[13] V. S. Pribiag, I. N. Krivorotov, G. D. Fuchs, P. M. Braganca, O. Ozatay, J. C. Sankey, D. C. Ralph, and R. A. Buhrman, Nat. Phys. **3**, 498 (2007).
[14] B. C. Choi, J. Rudge, E. Girgis, J. Kolthammer, Y. K. Hong, and A. Lyle, Appl. Phys. Lett. **91**, 022501 (2007).
[15] Y.-S. Choi, S.-K. Kim, K.-S. Lee, and Y.-S. Yu, Appl. Phys. Lett. **93**, 182508 (2008).
[16] W. Jin, H. He, Y. Chen, and Y. Liu, J. Appl. Phys. **105**, 013906 (2009).
[17] A. V. Khvalkovskiy, J. Grollier, A. Dussaux, K. A. Zvezdin, and V. Cros, Phys. Rev. B **80**, 140401 (2009).
[18] Y.-S. Choi, M.-W. Yoo, K.-S. Lee, Y.-S. Yu, H. Jung, and S.-K. Kim, Appl. Phys. Lett. **96**, 072507 (2010).
[19] E. Jaromirska, L. Lopez-Diaz, A. Ruotolo, J. Grollier, V. Cros, and D. Berkov, Phys. Rev. B **83**, 094419 (2011).
[20] Y. Gaididei, V. P. Kravchuk, and D. D. Sheka, Int. J. Quantum Chem. **110**, 83 (2010).
[21] J. C. Slonczewski, J. Magn. Magn. Mater. **159**, L1 (1996).
[22] L. Berger, Phys. Rev. B **54**, 9353 (1996).
[23] J. C. Slonczewski, J. Magn. Magn. Mater. **247**, 324 (2002).
[24] W. Thomson, *Mathematical and Physical Papers, Hydrodynamics and General Dynamics*, Vol. 4 (Cambridge University Press, Cambridge, UK, 1910), p. 563.
[25] A. A. Abrikosov, Rev. Mod. Phys. **76**, 975 (2004).
[26] R. J. Donnelly, *Quantized Vortices in Helium II: Cambridge Studies in Low Temperature Physics*, Vol. 3 (Cambridge University Press, Cambridge, UK, 1991).
[27] A. L. Fetter, Rev. Mod. Phys. **81**, 647 (2009).
[28] G. Ruben, M. J. Morgan, and D. M. Paganin, Phys. Rev. Lett. **105**, 220402 (2010).
[29] S. Komineas and N. R. Cooper, Phys. Rev. A **85**, 053623 (2012).
[30] A. Dreischuh, S. Chervenkov, D. Neshev, G. G. Paulus, and H. Walther, J. Opt. Soc. Am. B **19**, 550 (2002).
[31] S. A. Eastwood, A. I. Bishop, T. C. Petersen, D. M. Paganin, and M. J. Morgan, Opt. Express **20**, 13947 (2012).
[32] J. Xavier, S. Vyas, P. Senthilkumaran, and J. Joseph, Appl. Opt. **51**, 1872 (2012).
[33] U. K. Rößler, A. N. Bogdanov, and C. Pfleiderer, Nature **442**, 797 (2006).
[34] S. Mühlbauer, B. Binz, F. Jonietz, C. Pfleiderer, A. Rosch, A. Neubauer, R. Georgii, and P. Böni, Science **323**, 915 (2009).
[35] X. Z. Yu, Y. Onose, N. Kanazawa, J. H. Park, J. H. Han, Y. Matsui, N. Nagaosa, and Y. Tokura, Nature **465**, 901 (2010).
[36] X. Z. Yu, N. Kanazawa, Y. Onose, K. Kimoto, W. Z. Zhang, S. Ishiwata, Y. Matsui, and Y. Tokura, Nat. Mater. **10**, 106 (2011).
[37] D. Solenov, D. Mozyrsky, and I. Martin, Phys. Rev. Lett. **108**, 096403 (2012).

[38] O. M. Volkov, V. P. Kravchuk, D. D. Sheka, and Y. Gaididei, Phys. Rev. B **84**, 052404 (2011).

[39] Throughout, we denote the two-dimensional indexes by Latin letters while the three-dimensional indexes are denoted by Greek letters.

[40] V. Sluka, A. Kákay, A. M. Deac, D. E. Bürgler, R. Hertel, and C. M. Schneider, J. Phys. D **44**, 384002 (2011).

[41] A. I. Akhiezer, V. G. Bar'yakhtar, and S. V. Peletminski, *Spin Waves*, edited by G. Höhler (North-Holland, Amsterdam, 1968).

[42] N. Papanicolaou and T. N. Tomaras, Nucl. Phys. B **360**, 425 (1991).

[43] "The Object Oriented MicroMagnetic Framework", developed by M. J. Donahue and D. Porter mainly, from NIST. We used the 3D version of the 1.2α4 release.

[44] R. Hertel and C. M. Schneider, Phys. Rev. Lett. **97**, 177202 (2006).

[45] A. Yamaguchi, S. Nasu, H. Tanigawa, T. Ono, K. Miyake, K. Mibu, and T. Shinjo, Appl. Phys. Lett. **86**, 012511 (2005).

[46] J. Torrejon, G. Malinowski, M. Pelloux, R. Weil, A. Thiaville, J. Curiale, D. Lacour, F. Montaigne, and M. Hehn, Phys. Rev. Lett. **109**, 106601 (2012).

[47] M. Kläui, M. Laufenberg, L. Heyne, D. Backes, U. Rudiger, C. A. F. Vaz, J. A. C. Bland, L. J. Heyderman, S. Cherifi, A. Locatelli, T. O. Mentes, and L. Aballe, Appl. Phys. Lett. **88**, 232507 (2006).

[48] T. Ishida, T. Kimura, and Y. Otani, Phys. Rev. B **74**, 014424 (2006).

[49] A. R. Muxworthy, D. J. Dunlop, and W. Williams, J. Geophys. Res. **108**, 2281 (2003).

[50] G. Mihajlovic, M. S. Patrick, J. E. Pearson, V. Novosad, S. D. Bader, M. Field, G. J. Sullivan, and A. Hoffmann, Appl. Phys. Lett. **96**, 112501 (2010).

[51] Y. Gaididei, T. Kamppeter, F. G. Mertens, and A. Bishop, Phys. Rev. B **59**, 7010 (1999).

[52] Since the damping plays an important role for the noise-temperature relation,[51] it is necessary to take into account an additional effective damping, which is introduced by the the spin current by itself (see Sec. IV).

[53] J.-G. Caputo, Y. Gaididei, V. P. Kravchuk, F. G. Mertens, and D. D. Sheka, Phys. Rev. B **76**, 174428 (2007).